Correlating Hot Deformation Parameters with Microstructure Evolution During Thermomechanical Processing of Inconel 718 Alloy

CHIRAG GUPTA, JYOTI S. JHA, BHAGYARAJ JAYABALAN, RAJAT GUJRATI, ALANKAR ALANKAR, and SUSHIL MISHRA

Hot compression tests were conducted to determine the processing window for deformation of solutionized Inconel 718 over a range of high temperature and strain rate. Hot working map based on the dynamic material model was developed to establish the hot-processing regime. Maximum hot deformation efficiency within the processing regime is marked by the dynamic recrystallization, whereas an instability regime exhibits the highly deformed grains with shear bands. Further, selected deformed specimens were aged at 750 °C for 8 hours. Using electron back scattered diffraction and microhardness analyses, different microstructural properties such as grain size, twin fraction, grain average misorientation, and hardness were correlated. For deformed specimens, it was found that hardness is a function of misorientation and grain size. However, after aging treatment, hardness for all the specimens was found to lie in the range of 400 to 425 HV. Further, through transmission electron microscopy analysis, it was confirmed that deformed specimens are devoid of any precipitates while the deformed specimens followed by aging showed γ'' precipitates. Thus, the lack of correlation between the hardness and the grain size in the aged specimen was due to evolution of precipitates.

I. INTRODUCTION

INCONEL 718 is extensively used in gas turbine engine components because of its excellent mechanical properties and corrosion resistance at elevated temperatures.[1,2] High-temperature properties in this alloy are achieved by precipitation and solid solution hardening.[3,4] The most common precipitates in this alloy are γ' (Ni$_3$ (Al, Ti)—FCC), γ'' (Ni$_3$Nb—BCT) and δ (Ni$_3$Nb—orthorhombhic).[5,6] Yuan *et al.*[7] in their work reported that the presence of γ'/γ'' precipitates in the material enhances the peak stress during hot deformation. In contrast, the presence of δ precipitates not only reduces the peak stress but also provides higher softening. Thus, the existence of these precipitates significantly impacts the hot deformation behavior of Inconel 718.

Agnoli *et al.*[8] correlated the stored energy and grain growth mechanism during annealing near sub-solvus temperature (985 °C) of Inconel 718. They found that in the absence of stored energy grain size remains stable during annealing, which is controlled by δ-phase precipitates. On the other hand, a significant grain growth with bimodal distribution was observed in the specimen subjected to deformation prior to true strain < 0.1, whereas a homogeneous grain growth was observed for true strain > 0.1. Moreover, Azarbarmas *et al.*[9] in their study demonstrated that high-strain and temperature favor dynamic recrystallization (DRX) whereas a high deformation rate inhibits DRX. In addition, Inconel 718 has low stacking fault energy and therefore, it is susceptible to DRX during the hot working.[10,11] In general, DRX is the major flow-softening mechanism and it is largely employed to control the microstructure in a wide range of temperatures and strain rates in Inconel 718.[12–14] High-temperature deformation is a widely used processing methods for forming Inconel 718. However, the deformation process at high temperatures and high strain are likely to produce undesirable manifestations of

CHIRAG GUPTA, JYOTI S. JHA, ALANKAR ALANKAR, and SUSHIL MISHRA are with the Department of Mechanical Engineering, Indian Institute of Technology Bombay, Mumbai, India. Contact e-mail: sushil.mishra@iitb.ac.in BHAGYARAJ JAYABALAN is with the Department of Materials Science and Engineering, Indian Institute of Technology Kanpur, Kanpur, India. RAJAT GUJRATI is with the National Centre for Aerospace Innovation and Research, Indian Institute of Technology Bombay, Mumbai, India.

microstructure in the form of microvoids at intergranular particles, shear band formation and flow localization *etc*.[15,16] Therefore, a processing window in terms of strain rate ($\dot{\varepsilon}$) and temperature (T) for microstructure control is required. The concept of processing maps has evolved in the last couple of decades relating the processing parameters and the microstructures.

Wray[17] firstly formularized the failure mechanism in high-temperature tensile deformation by considering the strain rate *vs* temperature maps. The comprehensive quantitative approach to determine a processing window for high temperature and deformation was described by Raj.[18] Later, Prasad *et al.*,[19] Murty *et al.*,[20] Malas and Seetharaman,[21] Semiatin and Lahoti,[22] and Montheliate *et al.*[23] suggested different approaches to develop the processing windows ($\dot{\varepsilon}, T$). Xiong *et al.*[24] performed a comparative study of various instability criteria. Processing map proposed by Prasad *et al.*[19] based on a dynamic material model is extensively employed for hot working. Various studies conducted on the hot deformation of Inconel 718 have established a good correlation between experimental flow, unstable zones and models. A database of this can be found in the work of Prasad *et al.*[25] It has been observed that the maximum efficiency in a wide range of temperatures and strain rates is achieved by DRX.[26–28]

In the past, many researchers have extensively studied the hot deformation behavior of solutionized and aged Inconel 718.[29–32] In addition to this, many other studies on aging behavior of Inconel are available.[33–35] In practice, the processing route usually involves hot deformation and then aging to optimize the microstructure and its mechanical behavior. Very few studies have been performed on the microstructure evolution after deformation and aging in Inconel 718.[36,37] Studies conducted on nickel super alloy PER 72 by Bozzolo *et al.*[38] found that the final microstructure obtained after annealing depends upon the former straining cycle. The objective of the study was to determine the processing window of solutionized Inconel 718 using the model proposed by Prasad *et al.*[19] Further deformed specimens were selected for aging treatment such that a wide range of possible microstructure conditions could be analyzed. Through an extensive electron back scattering diffraction (EBSD) and microhardness analysis, for both deformed and deformed-aged specimens, microstructure–property relations were studied. Transmission electron microscopy (TEM) analysis was performed to gain further insight into the hardening of the precipitates. It was found that different deformed microstructures show different aging behavior of the material.

II. EXPERIMENTAL

Commercially available Inconel 718 was procured in the form of a 25 mm diameter extruded rod. The chemical composition of the procured Inconel 718 was determined using wet chemical analysis and is shown in Table I. For the hot compression tests, cylindrical specimens of 15 mm in height and 10 mm in diameter were machined using a wire electrical discharge machining (EDM). These specimens were vacuum sealed (10^{-5} bar) to prevent oxidation and heat treated in a temperature-controlled ($\pm$ 2 °C) muffle furnace. The specimens were completely solutionized at 1040 °C for 2 hours followed by water quenching. Hot compression tests were conducted on a computer-controlled Gleeble™ 3800 thermomechanical simulator in displacement control mode. A constant temperature was maintained throughout the specimen by electric resistance heating. The temperature of the specimen was measured using a chromel–alumel thermocouple spot welded to the middle of the specimen surface. A high-temperature inorganic ceramic adhesive cement (SYALUCEM—2) was applied on the welded spot and cured for 10 to 12 hours for better bonding. This method of bonding retains the thermocouple intact during the hot deformation and high-strain rate at an elevated temperature. The thermocouple was remained intact in most of the conditions during the deformation. For a few conditions at high temperature and high-strain rate, the thermo couple got detached. In such cases, the tests were repeated for better accuracy. At temperatures below 1000 °C, two layers of graphite and at temperatures above 1000 °C a tantalum layer was used as a lubricant between anvil and specimen. The specimens were heated up to deformation temperature at the rate of 5 °C s^{-1}. For uniform temperature, the specimens were soaked for 5 minutes at the deformation temperature before the compression test. The specimens were deformed in the temperature range of 900 °C to 1100 °C at an interval of 50 °C and at strain rates of 0.001, 0.01, 0.1, 1 and 10 s^{-1}. All the specimens were deformed up to 50 pct height reduction (0.69 true strain). Immediately after deformation, the specimens were subjected to forced air cooling.

All the specimens obtained after the compression tests were sectioned parallel to the compression axis into two halves. Based on the microstructure analyses, one split half of the deformed specimens at strain rate of 0.01 and 1 s^{-1} were aged at 750 °C for 8 hours. All the deformed and aged specimens were prepared for microstructural analysis using the standard metallography technique. Specimens were manually polished on silicon carbide polishing papers of grid size ranging from 300 to 2500. These specimens were then polished for 30 minutes using 0.04 μm particle sized Active Oxidant Polishing

Table I. The Chemical Composition of the Inconel 718 Used in the Current Study

Element	Ni	Cr	Nb	Mo	Al	Ti	Co	C	Fe
Weight Percent	53.65	18.10	5.18	3.01	0.51	0.89	0.85	0.05	Bal.

Suspension (OPS). In spite of the double layer of graphite, a bulging is observed in the specimen after the hot deformation, which leads to the inhomogeneous deformation. The microstructure analysis is performed on center region in the specimen where maximum deformation is observed.[39]

For microstructure analysis, EBSD data were acquired using OXFORD HKL system mounted on FEG Zeiss SEM Gemini 300. All the EBSD maps were obtained from the maximum-strained zone *i.e.*, the center of the specimens. EBSD scans were acquired using the step size of 0.8 μm or lower with the binning size of 4 × 4. EBSD data analysis was performed using commercially available TSL OIM™ orientation imaging software. The data were analyzed to calculate microstructural parameters such as average grain diameter size, grain average misorientation (GAM) and twin boundary fraction. All the results and analyses are reported in this work with a minimum Confidence Index of 95 pct.

Microhardness measurements were performed to get an insight into the hardness correlation with microstructure evolution. Microhardness data were acquired from a table top Shimadzu made HMV-2 hardness tester equipped with a square-based pyramid indenter. All hardness readings were acquired at a load of 9.8 N with a dwell time of 10 seconds and ten readings were taken from the center of the specimen. The indenter size for 10 N load was approximately 70 to 80 micron.

TEM analyses were carried out on the selected deformed and aged specimens. To prepare specimens for TEM analysis, a thin section of about 500 to 700 μm was initially sliced from the bulk specimen by a slow speed Isomet cutter. Then the sliced discs were mechanically thinned down to 100 to 120 μm using various grades of SiC emery sheets. Twin jet electro-polishing techniques were used to obtain the electron transparent thin region. Electrolyte containing 10 pct perchloric acid and 90 pct methanol was used for electro-polishing.

During polishing, the temperature of − 30 °C and potential of 24 V were followed. The FEI, Tecnai T20 tungsten-based TEM was used for microstructural analysis.

III. RESULTS AND DISCUSSION

A. Heat Treatment

Thermomechanical processing was conducted on solutionized specimens (Figure 1(b)) to capture the effect of microstructural parameters on the deformation behavior of Inconel 718 in the absence of precipitates. Some of the studies show hot deformation behavior at precipitate-hardened condition.[29,40] However, in standard industrial practice, initial hot deformation is done at the solutionized condition.[41,42] Therefore, solutionizing heat treatment was adopted to dissolve all the precipitates present in the as-received condition. Image quality (IQ) maps [43] of as-received and solutionized condition of Inconel 718 used in the current study are shown in Figures 1(a) and (b). Twin boundary having $(\sum 3(\langle 111\rangle, 60 \deg))$ orientation relationship with the maximum deviation of 5 deg is also plotted on IQ maps and shown as a red line in the Figure 1. The as-received specimen shows inhomogeneous grain size distribution with a very low fraction of twin boundary. The GAM of the as-received material is 1.26 deg which indicates existence of the local strain. The hardness value corresponding to the solution treated specimen is 214 ± 2 HV, which is close to the precipitates free Inconel 718 specimen.[34] Inconel 718 obtained after solutionizing is precipitate-free with a large fraction of annealing twins.[44] The average grain size diameter (area fraction method) was measured to be ~ 56 μm and twin boundary fraction is ~ 0.56. After solutionizing, GAM decreases to 0.29 and local strain is minimal. High-temperature deformation studies at different
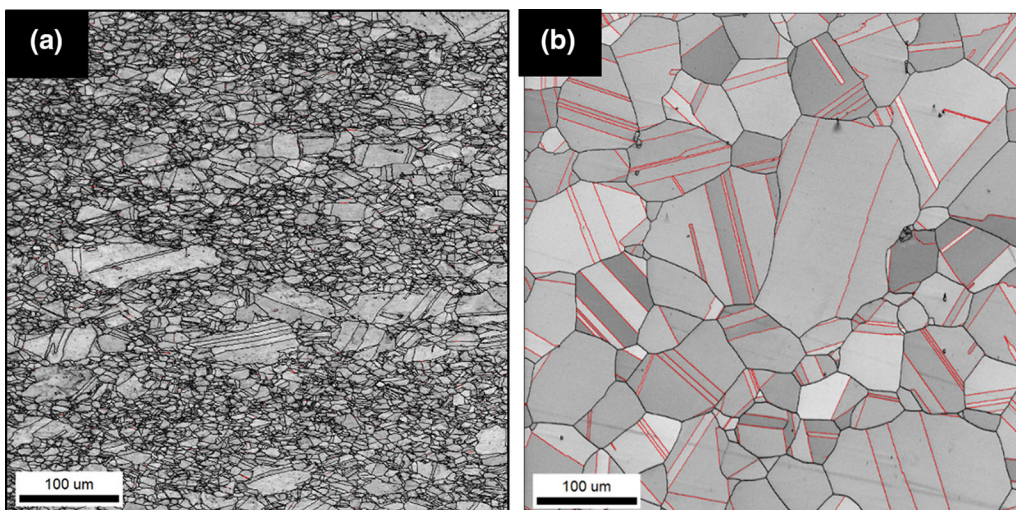

Fig. 1—IQ maps of (*a*) as-received and (*b*) solutionized Inconel 718 used in the current study. Grain and twin boundaries are marked in black and red color, respectively.

Table II. Flow Stress (MPa) Data at Various Deformation Conditions

True Strain	Strain Rate (s^{-1})	Temperature				
		900 °C	950 °C	1000 °C	1050 °C	1100 °C
0.1	0.001	206	137	103	85	63
	0.01	305	233	182	140	106
	0.1	292	332	270	212	170
	1	326	327	355	294	254
	10	378	349	408	390	365
0.2	0.001	217	144	94	79	57
	0.01	317	239	180	138	99
	0.1	419	369	279	219	172
	1	449	449	362	294	252
	10	504	483	514	432	370
0.3	0.001	215	139	87	71	51
	0.01	311	234	169	127	90
	0.1	465	369	272	210	164
	1	544	458	346	289	246
	10	605	583	528	424	355
0.4	0.001	205	131	81	64	47
	0.01	302	227	154	116	80
	0.1	473	364	259	199	152
	1	566	450	323	278	233
	10	657	614	506	403	336
0.5	0.001	192	121	76	60	45
	0.01	299	219	142	109	72
	0.1	468	355	242	182	142
	1	555	435	308	266	224
	10	663	598	467	376	315
0.6	0.001	179	112	74	58	44
	0.01	274	211	134	102	69
	0.1	456	341	230	174	132
	1	536	421	290	257	220
	10	640	567	436	352	298

temperatures and strain rates were conducted in a solutionized condition where grains are mostly strain free, without precipitates and having more than 50 pct twin boundaries.

B. Stress–Strain Response and Hot Compressed Microstructures

Flow stress at the true strain level of 0.1 to 0.6 with the increment of 0.1 obtained from the hot compression test at an above-mentioned range of temperature and strain rate condition is given in Table II. The complete stress–strain plots are given elsewhere.[45]

At constant temperature, flow stress increases with increase in strain rate. However, at a constant strain rate, flow stress decreases with increasing temperature. The flow stress increases initially at lower strain rates due to the work hardening, which is reported in Reference 44. Immediately after reaching the peak stress, flow stress decreases with further strain. This typical behavior of decreasing flow stress is attributed to dislocation annihilation/recrystallization and is characteristic of flow softening.[46] Though dynamic recovery (DRV) is activated after the initial stage (work hardening) of hot deformation of Inconel 718, the primary flow-softening mechanism is attributed to DRX.[32,47]

Since, the Inconel 718 has lower stacking fault energy, the recovery process will be slower compared to the DRX after reaching the critical strain.[7] Moreover, the hot deformation activation energy based on the flow stress curve is a good measure to predict the softening mechanism such as DRX/DRV. When the activation energy of the hot deformation is higher than the self-diffusion activation energy, the deformation process is mostly governed by the DRX; otherwise the process is DRV.[48] The average deformation activation energy calculated for this alloy is 364 kJ mol^{-1}, which is much higher than the self-diffusion (250 kJ mol^{-1}) and suggests that the deformation is mainly dominated by DRX.[45]

A comprehensive microstructure analysis was carried out using EBSD to understand the microstructure evolution for the wide range of $\dot{\varepsilon}, T$. The analysis shows the distinct evolution of the microstructure depending on the deformation conditions. High-temperature deformation (> 1000 °C) evidences the complete DRX for all the deformation strain rates (shown by black arrow in Figure 2). However, the low strain rate deformation (0.001 to 0.01 s^{-1}) produces coarser grain structure as compared to the higher strain rate deformation. This observation suggests that the elevated temperature deformation at a lower strain rate induces the DRX early (lower strain) and provides enough duration to
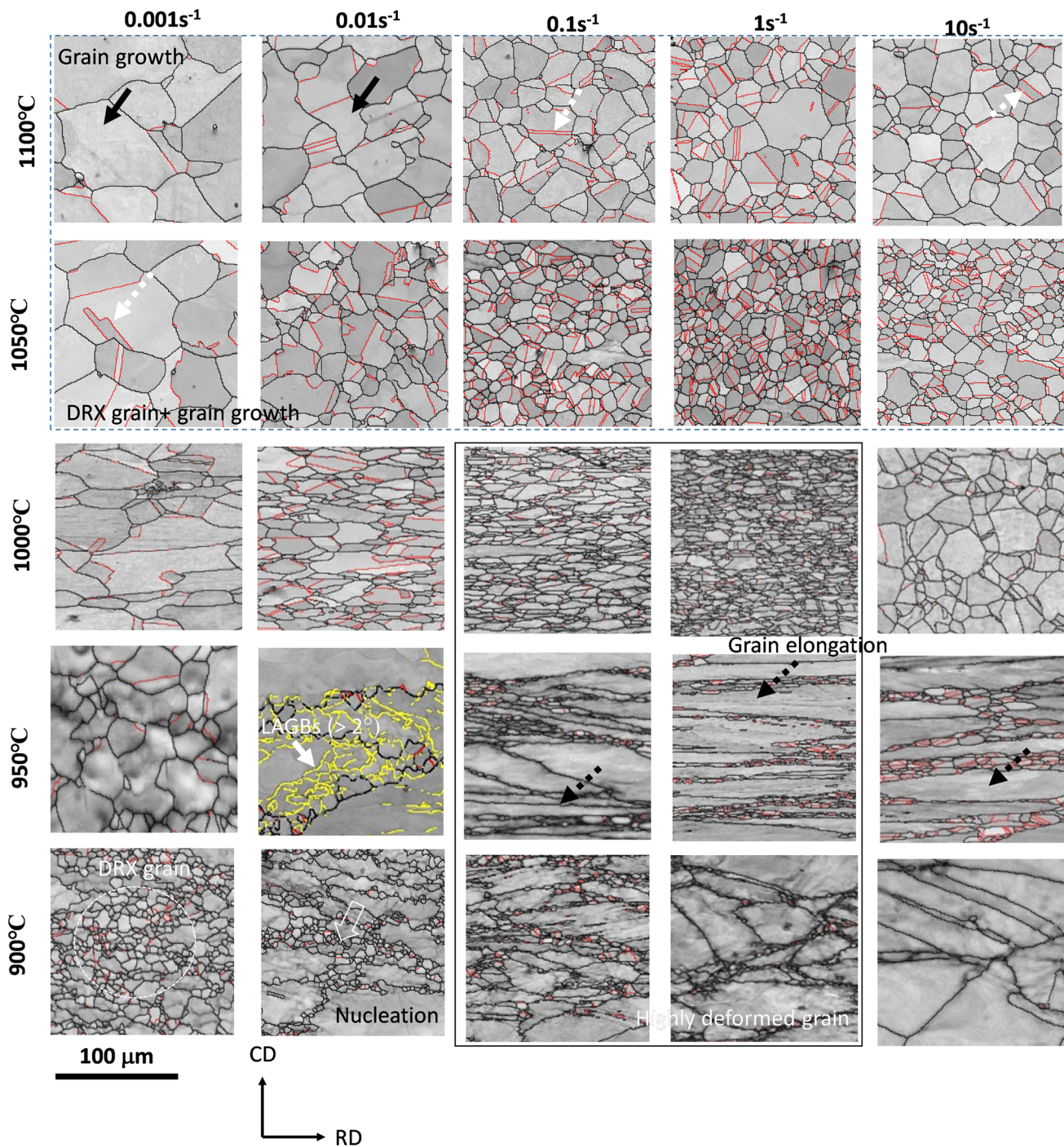
Fig. 2—IQ map after 50 pct deformation: variation with strain rate and temperature (CD is compression direction and RD is radial direction).

promote the grain growth. As a result, the grains structure becomes coarser in the lower strain deformation. In the case of higher strain deformation (0.1 to 1.0 s^{-1}), although the DRX is prevalent but the grains sizes are relatively smaller because of short period of deformation.

The microstructure evolution was observed to be slightly different when the sample deformed at 1000 °C. The microstructure shows that the selected deformation temperature is enough to induce the DRX for different strain rates. In comparison to the elevated temperature where DRX grains were more equiaxed, these are more elongated in the radial direction. At intermediate temperature and strain rate (1000 °C and 1 s^{-1}), the microstructure (Figure 3(d)) shows the signature of the deformation characteristics (elongated grains); however, the grains are observed to be newly developed suggesting that the nearly complete DRX occurs even at a lower strain.
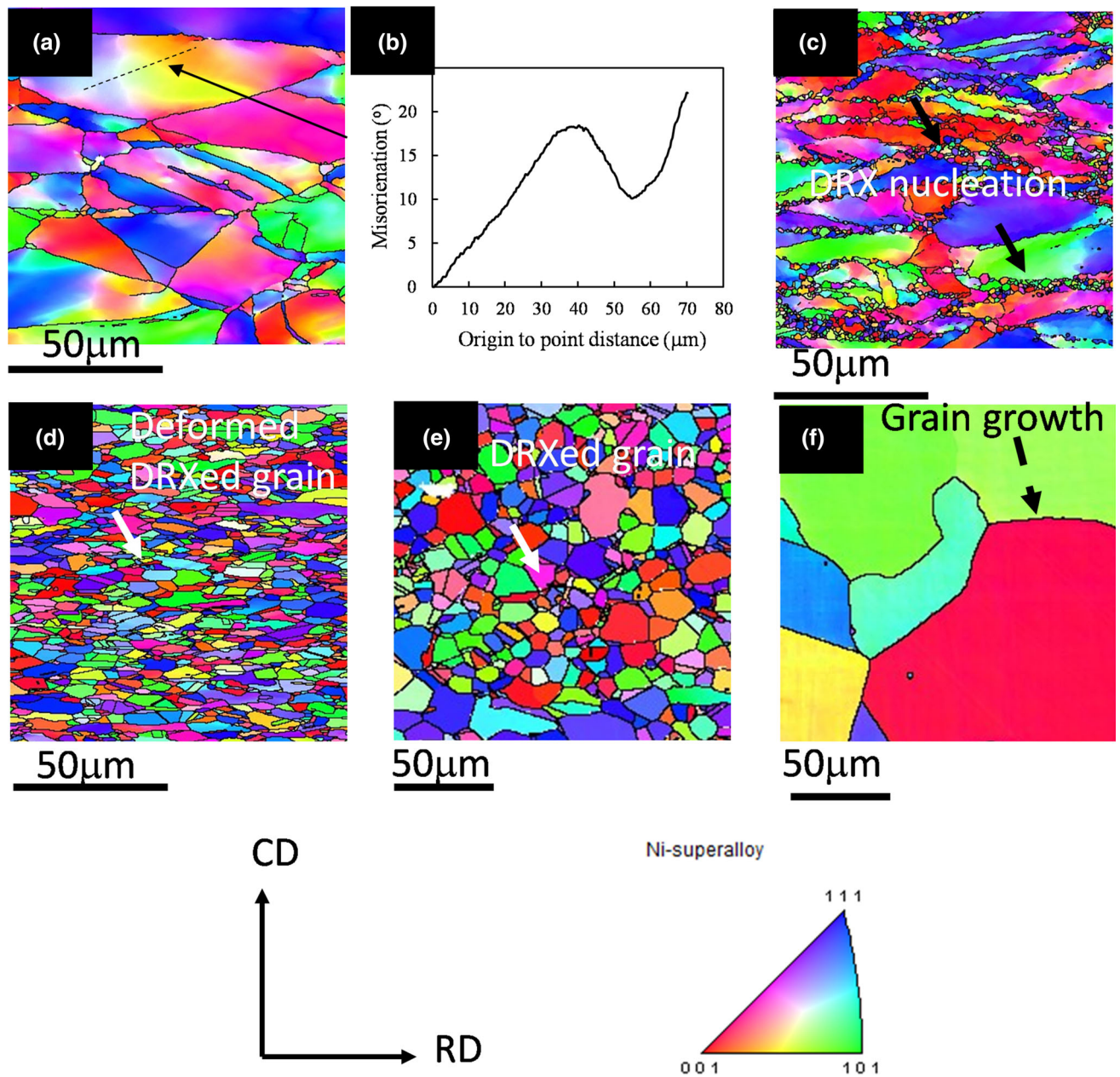
Fig. 3—Different stages of microstructure evolution (*a*) deformed microstructure, (b) misorientation profile across the red line marked in (a), (*c*) recrystallized grains at grain boundaries, (*d, e*) completely recrystallized grains, (*f*) DRX grain with extreme grain growth.

The microstructure evolution is distinctly different in the low temperature (< 1000 °C) as it shows only partial or no DRX. The deformation at lower temperatures (900 °C and 950 °C) and lesser strain rates (0.001 and 0.01 s^{-1}) lead to simultaneous occurrence of severe deformation and DRX of the grains. As a result, the grain boundary serration and DRX grain nucleation are prevalent in the sample deformed with lower strain rate of 0.01 s^{-1} at 900 °C and 950 °C. Microstructure analysis at the lower temperature and strain rate, (900 °C and 0.01 s^{-1}), exhibits the grain boundary nucleation (shown by hollow arrow in Figure 2) along with an extensive low angle boundary formation (marked by the yellow boundaries > 2° in Figure 2). Lower strain rate deformation favors the occurrence DRX (encircled in Figure 2) as it was seen in high-temperature deformation. However, the signature of DRX is reduced with increasing strain rate (> 0.01 s^{-1}). The microstructure of the high-strain rate deformed sample shows significantly less DRX grains and the grain structure appears to be more elongated (shown by dotted black arrow in Figure 2) and resembles the deformed structure. Nevertheless, the low IQ of these grains also indicates that the grains possess enormous internal-stored energy during the deformation.

In all the cases, it is interesting to note that the DRX process in terms of nucleation and growth are significant at a very high-strain rate of 10 s^{-1}. Regardless of the deformation temperature, the microstructure development (DRX grains) is significant with lower strain rate and reduces with increasing strain rate. At higher strain rates, the DRX grains again become coarser as observed in the lower strain rate deformation. Similar observations have been reported by Guo et al.,[14] and Chen et al.[32] during hot deformation of nickel-based super alloys. It has been suggested that at a very high-strain rate, the deformation induces severe dislocation density and a significant amount of adiabatic heat in the material.[9] The high-dislocation density increases the internal-stored energy that favors the occurrence of DRX. The simultaneous occurrence of defect generation and adiabatic heat rise develops the coarser grain structure at higher strain rate deformation in all the deformed sample regardless of the deformation temperature.

Based on the microstructure evolution at lower and higher temperature, another interesting observation that came to light is twin formation. The pre-existing twin boundaries $(\sum 3(\langle 111\rangle, 60°)$ type) in the starting microstructure disappears after deformation. However, it emerges again in the DRX grains (shown by the white dotted arrow) after deformation and are dominant at elevated temperature deformation. Existing annealing twin boundaries during deformation are indexed (red boundaries in Figure 2) as regular boundaries during EBSD analysis due to large in-grain misorientation development.[49]

From the inverse pole figure (IPF) maps shown in Figure 3, various stages of microstructure evolution and DRX can be realized. At a lower temperature (900 °C) and high-strain rate (10 s^{-1}), grains are highly deformed and no DRX is observed (Figure 3(a)). Therefore, high in-grain misorientation development can be observed and shown by the origin-to-point misorientation plot (Figure 3(b)) of the grain (dotted line marked in Figure 3(a)). As the strain rate is decreased (900 °C and 0.01 s^{-1}) proliferation of small DRX grains can be seen at the grain boundaries (Figure 3(c)). At intermediate temperature and strain rate (1000 °C and 1 s^{-1}), the microstructure (Figure 3(d)) shows the signature of the deformation characteristics (elongated grains); however, the grains are observed to be newly developed suggesting that the nearly complete DRX occurs even at a lower strain. At higher temperatures (1050 °C and 1100 °C) DRX occurs even at a very high-strain rate of 10 s^{-1} as sufficient activation energy is provided by temperature alone for DRX to occur (Figure 3e). If the specimen is allowed to remain at the higher elevated temperature (1100 °C) for a longer duration through slow deformation (0.001 s^{-1}) considerable grain growth occurs (Figure 3f).

To quantify the effect of temperature and strain rate on DRX, the DRX fraction corresponding to each of the deformation conditions was calculated and is shown in Figure 4. To accomplish this, grain size and GAM was used as cutoff criteria. The cutoff grain size was altered for different deformation conditions as DRX grain size may vary with combination of temperature and strain rate. However, the GAM value was considered less than 0.2 for the DRX grains.[50] Based on this calculation the DRX fraction with temperature and strain rate is plotted in Figure 4(a). Also, a colored contour map was plotted to show the extent of DRX grains at different deformation conditions using cubic spline fitting, as shown in Figure 4(b). The contour map clearly evidences the two distinct regions (red and blue), where the red region dominantly represents the DRX whereas the blue region demonstrates the highly deformed region. Two processing conditions, 'A' (1100 °C and 0.01 s^{-1}) and 'B' (950 °C and 0.1 s^{-1}) have been identified from the contour map (Figure 4(b)) to illustrate the extent of DRX. As observed by IQ maps (Figure 2) complete DRX is observed at higher
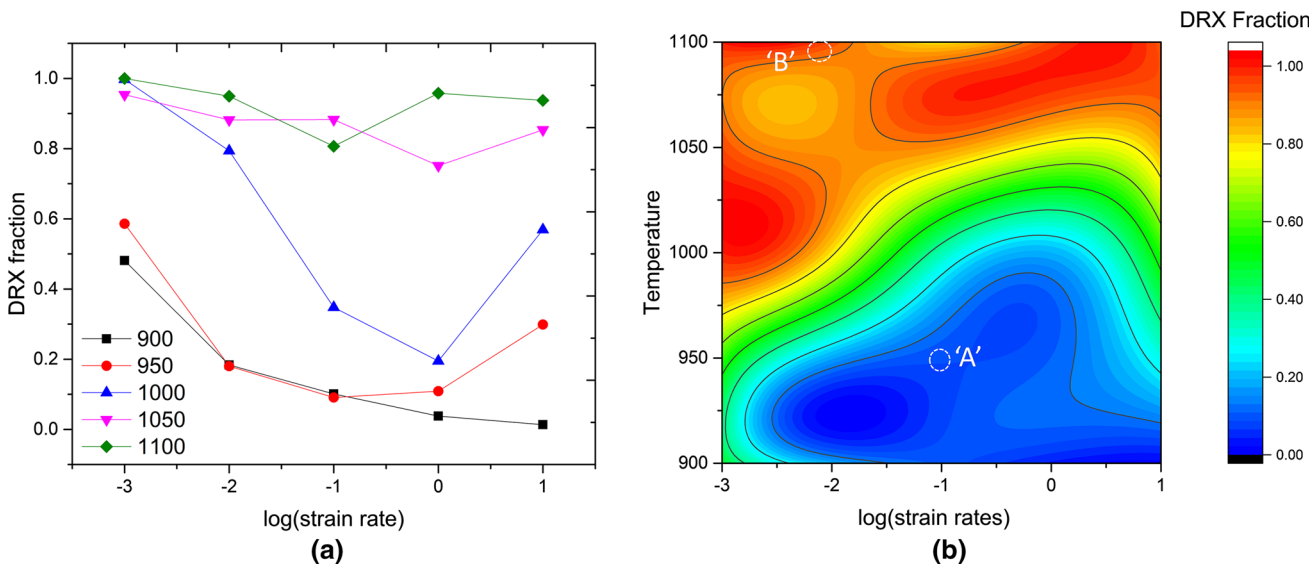

Fig. 4—DRX fraction, (*a*) variation with temperature and strain rate after 50 pct deformation, (*b*) color contour map based on cubic spline fit.

temperatures and it decreases with decrease in temperature. DRX is also a function of strain rate for temperatures below 1000 °C. As the strain rate increases, the DRX fraction decreases and at higher strain rate (10 s^{-1}) DRX fraction increases. Increase in DRX at higher strain rate is possibly due to higher adiabatic temperature rise. It has to be noted that the extent of DRX and grain size are dependent on strain rate and temperature. To achieve the desired or homogeneous microstructure after deformation a processing window needs to be identified. To correlate the microstructures obtained at different deformation conditions with processing parameters, a processing map was drawn considering dynamic material flow model proposed by Prasad et al.[19]

C. Processing Map

The most widely used theory for predicting the processing window is based on the dynamic material model given by Prasad et al.[19] This theory of predicting the unstable flow zone where hot deformation is most susceptible to cracks and unstable plastic flow is based on the principles of irreversible thermodynamics derived by Ziegler[51] for the first time in 1963. Building upon Ziegler's work Prasad et al.[19] derived that strain rate sensitivity, m, based model to determine processing conditions.

The total power (P) supplied externally in hot working can be divided into two components, power dissipated in plastic deformation ($G = \int_0^{\dot{\varepsilon}} \sigma d\dot{\varepsilon}$) and power dissipated for bringing microstructural changes ($J = \int_0^{\sigma} \dot{\varepsilon} d\sigma$).[19] These two power terms are represented as integral and are shown in Eq. [1]

$$P = \sigma\dot{\varepsilon} = \int\limits_0^{\dot{\varepsilon}} \sigma d\dot{\varepsilon} + \int\limits_0^{\sigma} \dot{\varepsilon} d\sigma, \qquad [1]$$

where σ is true stress and $\dot{\varepsilon}$ is strain rate. To evaluate the energy dissipated in bringing microstructural changes (J), a function describing the variation of flow stress with strain rate is needed. For this purpose, the power law describing the dynamic response of the material is used.

$$\sigma = K\dot{\varepsilon}^m, \qquad [2]$$

where K is material constant and m is strain rate sensitivity given by $m = d(ln\sigma)/d(ln\dot{\varepsilon})$.

Using Eq. [2], the second integral component of Eq. [1] (J) can be derived.

$$J = \left(\frac{m}{m+1}\right)\sigma\dot{\varepsilon}. \qquad [3]$$

The maximum possible power that can be dissipated in microstructural changes occurs at a strain rate sensitivity m = 1.[19] The efficiency η in hot deformation process is given as the ratio of the experimental value of power dissipated in microstructural changes to maximum possible value. In view of this definition, strain rate sensitivity m of flow stress turns out to be an important parameter that determines the efficiency of thermomechanical processing.

$$\eta = \frac{J}{J_{max}} = \frac{2m}{m+1}. \qquad [4]$$

Together with the efficiency map, the instability map derived from Ziegler criteria[51] determines the processing map. Stability criteria are given as

$$\frac{J}{\dot{\varepsilon}} > \frac{dJ}{d\dot{\varepsilon}}. \qquad [5]$$

Substituting Eqs. [4] in [5] determines the expression for stability value (ξ) and is given as

$$\xi = \frac{\partial \ln\left(\frac{m}{m+1}\right)}{\partial \ln \dot{\varepsilon}} + m > 0. \qquad [6]$$

The processing map combines the efficiency map based on the Prasad et al.[52] model and stability map based on Ziegler's criteria.[51] To construct the efficiency map, direct experimental data obtained from the hot compression test was used to compare the microstructure evolution at the end of deformation with processing maps.[19,21,25]

The entire process and formulation are discussed elsewhere.[52] At a particular true strain (say 0.6) and temperature (say 900 °C), stress values at various strain rates were fitted using cubic spline and strain rate sensitivity (m) as a function of strain rate as given in Eq. [2] was calculated. The same procedure was adopted to determine m at all the other five temperatures. Discrete values of variations of m at five different temperatures were interpolated through cubic spline to get a continuous variation. The 2D plot of the efficiency (η) (colored contour line with efficiency value) at a strain of 0.6 was plotted and is shown in Figure 5(a). Calculated m values were substituted in Eq. [6] to evaluate stability parameter (ξ) at 0.6 true strain and overlapped (color contour) on efficiency maps to obtain the complete processing map as shown in Figure 5(a).

From the efficiency contour of the processing map, it is clear that the maximum efficiency value of 0.4 corresponds to the lower strain rate. In these regions, it is evident from the IQ maps that partial DRX occurs at lower temperatures and complete DRX with uniform grain size occurs at higher temperatures. The region corresponding to the stable and unstable processing zones is also shown as colored contours and white region, respectively. The unstable zone observed in the processing map (white region) corresponds with the intermediate value of strain rate i.e. 0.1 s^{-1} and low temperature (up to 1000 °C). The locations indicated by 'A' and 'B' in Figures 4(b) and 5(a) represent the exclusively stable and unstable region, respectively. The stress–strain curve corresponding to the stable (1100 °C/
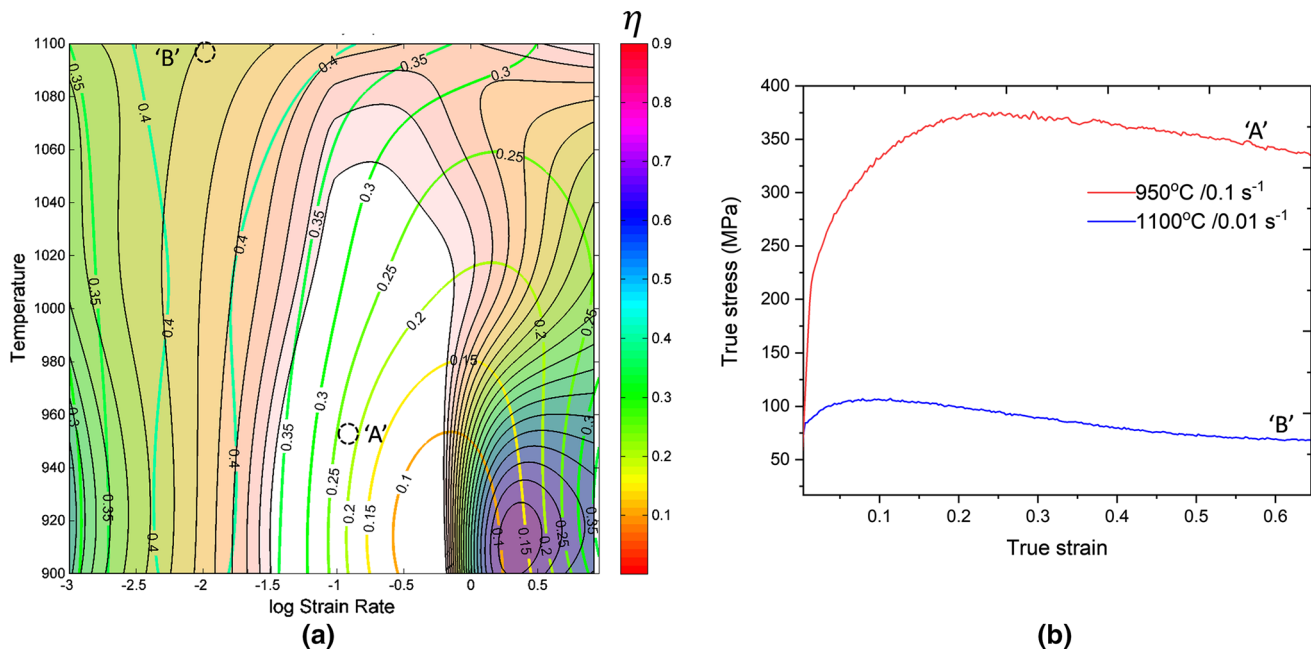
Fig. 5—(a) Processing map for Inconel 718 in the temperature range 900 to 1000 °C and strain rate 0.001 to 10 s^{-1} based on Prasad *et al.*'s[52] model and (b) the stress–strain plot corresponding to the stable (1100 °C/0.01 s^{-1}) and unstable (950 °C/0.1 s^{-1}) zones.

0.01 s^{-1}) and unstable zone (950 °C/0.1 s^{-1}) is plotted in Figure 5(b). It can be noted that in the stress–strain curve for 950 °C/0.1 s^{-1}, the hardening phase is too high (up to strain 0.2) along with the flow stress magnitude. This indicates that there is a significant accumulation of storage energy (dislocation) in the deformed grain. On the other hand, the flow stress for 1100 °C/0.01 s^{-1} is significantly less with a very low-hardening stage (< 0.03 strain). This implies that the deformation at elevated temperature and slow strain rate is governed by flow-softening mechanisms such as DRX. The processing map can be correlated with the IQ map of ESBD analysis. The IQ value for the unstable zone is very low and inhomogeneous microstructure is observed. Lower IQ value is an indication of strain localization or very high-dislocation density.[53] It has also been observed that all the grains are heavily deformed and almost no DRX is observed. In addition to this, highly deformed grains also show the presence of shear bands. Due to such highly strained or deformed microstructure, this zone is considered as an unstable zone as suggested by the processing map (Figure 5(a)).

The maximum efficiency in the processing map of Inconel 718 is mostly observed with the DRX grain development.[26–28] In the present work on Inconel 718 in solutionized condition (precipitate-free), maximum efficiency can be achieved at a high temperature and low-strain rate regime. The dissipation of energy mostly occurs by the DRX process and the stored energy is the driving force for DRX.[54] This energy is supplied externally through deformation and is stored in the form of GNDs.[54] This also corresponds to the theoretical prediction of the processing map which gives the

fraction of energy that goes into microstructure changes. Hot deformation at elevated temperatures and lower strain rates results into lowering the critical strain for the occurrence of DRX.[14,55,56] Moreover, grain growth after DRX is mainly dependent on stored internal energy.[54] The grain growth is slower at low temperatures, whereas it is faster at higher temperatures and low strain rates where the dislocation density is minimum.[12,13,40] This is also evident from the grain size variation with the temperature in the lower strain rate regime as shown in the IQ map in Figure 2. Therefore, optimum microstructure based on the processing map can be achieved in a wide range of temperature and strain rates.

It should be noted that the processing parameters ($\dot{\varepsilon}$, T) for hot deformation were designed using TTT diagram of Inconel 718, such that the precipitates were absent in the deformed specimen. The various microstructures were selected from microstructure map and aged further. Relationships have been established between the microstructure and property and discussed in the following section:

D. Aging of Deformed Specimens

Two regions of the processing map were chosen for further studies to understand the effect of aging on deformed specimens. These two regions mostly cover almost all different kinds of microstructure present in the whole processing map (Figure 2). These two regions correspond to a strain rate of 0.01 s^{-1} with highest efficiency (~ 0.4) and a strain rate of 1 s^{-1} with lowest efficiency (~ 0.1). Specimens deformed at strain rate 0.01 and 1 s^{-1} (at all the five different temperatures) were
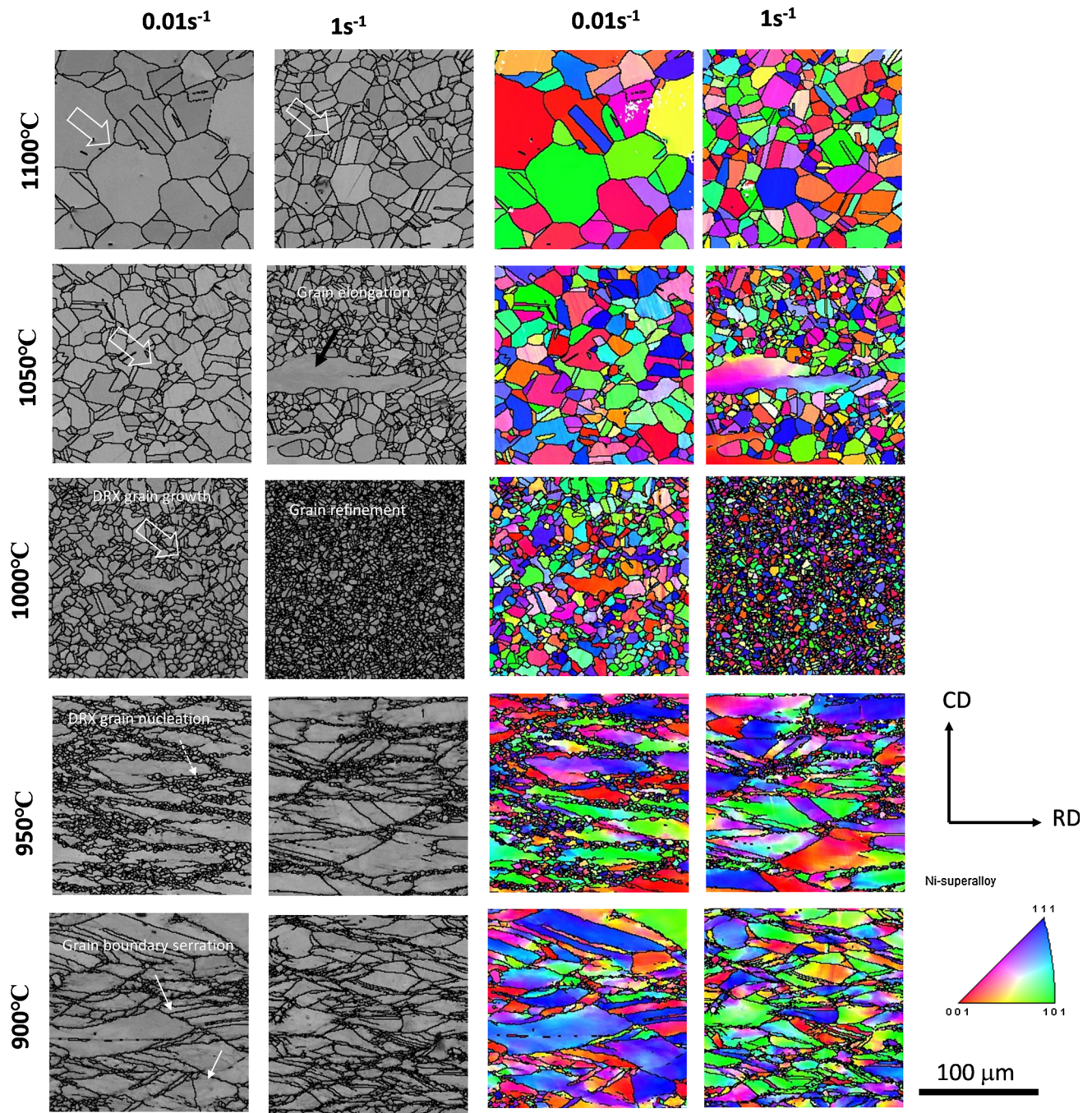
Fig. 6—IQ and IPF micrographs of deformed and aged specimens at temperature 900 °C, 950 °C, 1000 °C, and 1050 °C, and strain rate 0.01 and 1 s^{-1}.

aged at 750 °C for 8 hour and the corresponding IQ and IPF maps are shown in Figure 6.

Thus, almost no qualitative microstructure distinction between deformed and aged specimens at the same processing conditions was observed (as shown in IQ maps of deformed (Figure 2) and deformed + aged (Figure 6) specimens). Therefore, a systematic analysis of GAM, grain size distribution, twin boundary fraction and Vickers hardness, were performed to get an insight into the microstructural evolution of deformed and deformed + aged specimens.

E. *Microstructure–Property Relationship*

1. *Grain Size*

Different microstructural parameters are compared at strain rate 0.01 and 1 s^{-1} to get an insight into the effect of deformation on aging. In deformed specimens, there is very high variance in grain size due to the presence of small recrystallized grains and a deformed matrix at the same time. Thus, grain size area rather than grain size diameter was used as the comparison parameter. Figures 7(a) and (b) show grain size variation with
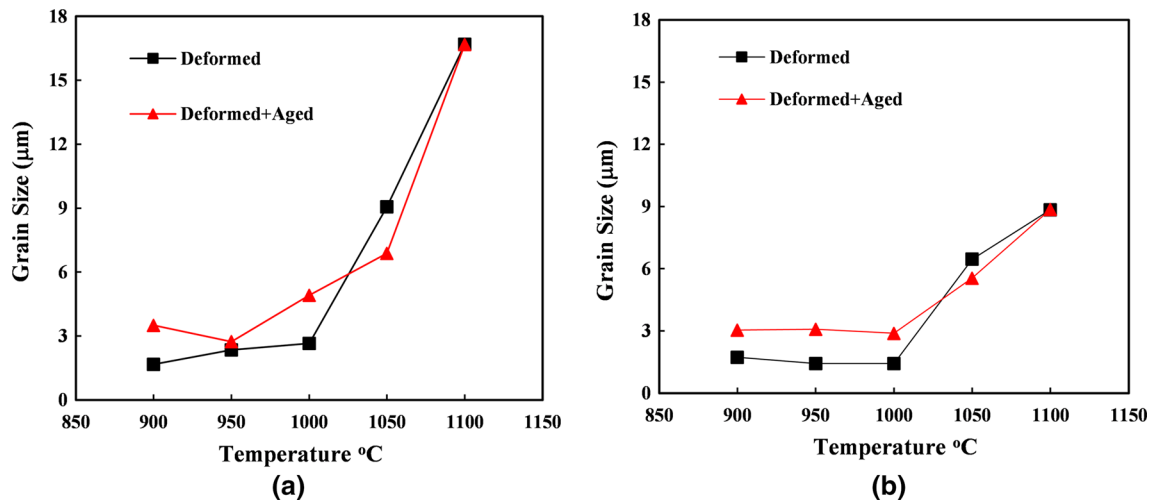
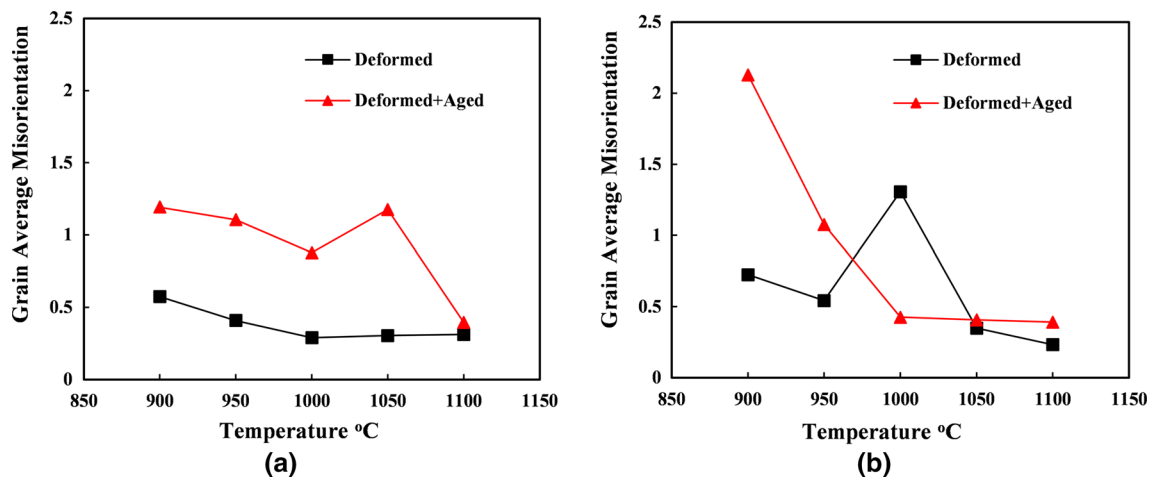Fig. 7—Variation of grain size with temperature at strain rate (*a*) 0.01 s^{-1}, (*b*) 1 s^{-1}.

Fig. 8—Variation of GAM with the temperature at strain rate (*a*) 0.01 s^{-1}, (*b*) 1 s^{-1}.

temperature at strain rates 0.01 and 1 s^{-1}, respectively. It is evident from the figure that at temperatures above 1000 °C, grain size increases very significantly and there is very slight variation of grain size after the aging treatment. The aging temperature was not enough for any significant recrystallization or grain growth. The slight variation in grain size mostly at a lower deformation temperature is because the stored energy or local strain is higher at this condition that may provide stored energy for recovery/ recrystallization or slight grain growth.

2. *GAM and Twinning*

It is expected that after deformation GAM will increase due to accumulation of dislocations and lattice rotation.[57] Deformation at higher temperatures may also involve softening mechanisms such as DRV and recrystallization of Inconel 718.[26–28,58] The misorientation development is also a function of strain rate.[40] It can be observed from Figures 8(a) and (b) that GAM is very low for the as-deformed specimen as compare to the deformed + aged specimens. The only exception is

the specimen deformed at 1000 °C with the strain rate of 1 s^{-1} where the trend gets reversed. At this condition, the grain size (Figure 7) is very small (2.65 *μ*m) after the deformation and almost no DRX grain (Figure 2) is observed (less than 20 pct). Due to very high-deformation GAM will increase and after the aging treatment GAM may have decreased. However, after aging treatment at 750 °C for 8 hour, GAM value is expected to decrease for all the deformation conditions but it increases significantly (Figures 8(a) and (b)). Precipitates are also an important factor in the increased misorientation after aging. The GAM value is already very low (less than 0.5 deg) after the hot deformation and it may not decrease after the aging treatment, since this GAM value is very close to the measurement error during EBSD data collection. The precipitates may cause lattice distortion and will increase the misorientation. This is a likely reason behind higher misorientation of the deformed + aged specimens.

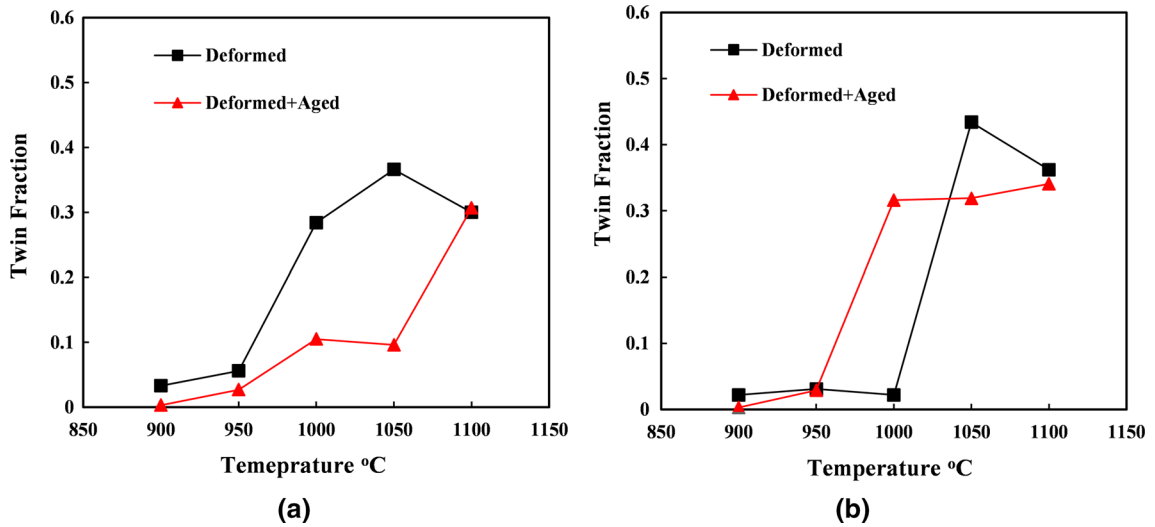It is also understood that misorientation development can have an effect on twin boundary fraction.[49] As

Fig. 9—Variation of twin boundary fraction with the temperature at strain rate (*a*) 0.01 s^{-1}, (*b*) 1 s^{-1}.
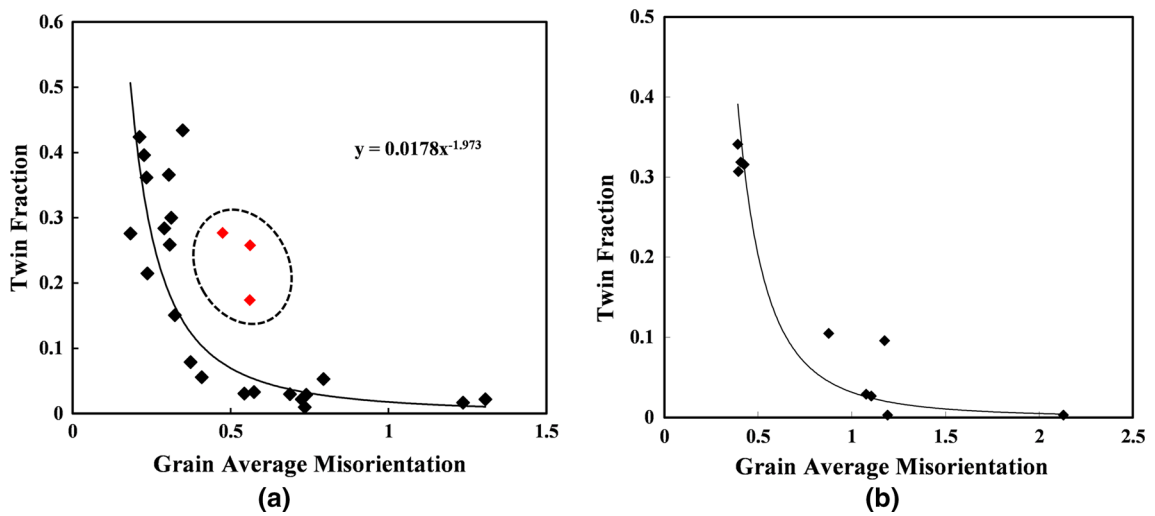

Fig. 10—Twin boundary fraction variation with GAM for (*a*) deformed specimens, encircled red legend indicates the deviation from the trend line, (*b*) deformed and aged specimens.

observed from Figures 9(a) and (b), twin fraction decreases for deformed and aged conditions for all the specimens except the specimen deformed at 1000 °C with the strain rate of 1 s^{-1}. This trend compares well with the development of misorientation after the aging treatment. Hence, a plot between GAM and twin boundary fraction was obtained for all deformed and deformed + aged conditions and shown in Figures 10(a) and (b) respectively. It is evident that as the GAM value increases, the twin fraction decreases, and it follows the power law curve. The three conditions showing maximum deviation in Figure 10(a) are shown in red. Deviation from the observed character may be due to abnormal grain growth as observed in the deformation condition of 1100 °C and 0.001 s^{-1}. The larger the grain size the higher the twin boundary fraction, since the fraction of high angle grain boundaries will decrease. Hence, it can be concluded that

misorientation development and decrease in twin fraction in the deformed + aged condition is due to precipitate formation. These precipitates will also have an effect on hardness of the specimen, as discussed in the following section.

3. *Microhardness*

Microhardnesses for all the twenty-five deformed specimens were measured and are shown in Figure 11. At a constant strain rate, hardness was found to decrease from the specimen deformed at 900 °C to 1100 °C. This is in correspondence with the fraction of DRX grains. From the DRX fraction map (Figure 4) it is clear that the DRX fraction increases from 900 °C to 1100 °C and finally at 1100 °C, fully recrystallized grains are obtained. Hardness measurements at a constant temperature with varying strain rates show that hardness value increases from 0.001 s^{-1} strain rate

and reaches a maximum at 0.1 or 1 s^{-1} and then further decreases at 10 s^{-1}. It can be inferred from the DRX fraction since the amount of DRX decreases at high-strain rate deformation.

Variation of hardness with grain size for all the 25 combinations of deformation states was plotted and found to follow a trend mathematically depicted as a power law as shown in Figure 12(a). The hardness value decreases with increasing grain size and is found to be maximum for 900 °C and 0.1 s^{-1} deformation condition. This observation follows the classical relation between grain size and hardness.[59] Hardness values of deformed + aged specimens increased almost twofold as compared to only deformed specimens. However, unlike deformed specimens where microhardness shows a power law relation with the grain size of specimen, hardness after aging was found to lie in the range of 400 to 450 HV, irrespective of grain size. As is clear from Figure 12(b), hardness of aged specimens was found to be independent of grain size.

It is clear that for specimens deformed at both 0.01 and 1 s^{-1} strain rates, aging treatment causes a significant increase in hardness as shown in Figures 13(a) and (b). After aging, hardness of specimens deformed at 0.01 s^{-1} was found to increase by about 125 HV (Figure 13(a)) as compared to only deformed specimens, while those specimens which were deformed at 1 s^{-1} after aging possessed hardness lying in the narrow range of 400 to 450 HV (Figure 13(b)) irrespective of the temperature at which they were deformed.

The higher hardness of the deformed + aged specimen indicates the formation of precipitates. The TTT diagram also suggests the formation of γ'' for the aged specimen.[34] It was found that the deformed + aged specimen hardness is significantly higher in comparison to the deformed specimen. Moreover, the relationship between hardness and grain size is very prominent and it shows higher hardness for low-grain size (which is expected). Considering the above observation, it was concluded that the presence of precipitates during the deformation at the lowest temperature and strain rate is either very low (insignificant) or absent. To confirm this, the precipitation behavior of selected specimens was examined using TEM and discussed in the following section:

From microstructural observations, it was found that misorientation increased after aging as compared to deformed specimens and a direct correlation of misorientation with twinning was observed for both deformed and deformed + aged condition. A power law relation with grain size and hardness could be established for the deformed specimens. However, for the deformed and aged specimens, no such correlation could be established. To get an insight into the microstructural changes, TEM analysis was performed. Two specimens (i) deformed at 1050 °C and 0.1 s^{-1} and (ii) deformed (at 1050 °C and 0.1 s^{-1}) and aged at 750 °C for 8 hours were subjected to TEM analysis and the corresponding TEM images are shown in Figures 14 and 15 respectively.

Figure 14 shows the montage of TEM micrographs and the selected area diffraction pattern (SADP) of the specimen deformed at 1050 °C and 0.1 s^{-1}. The
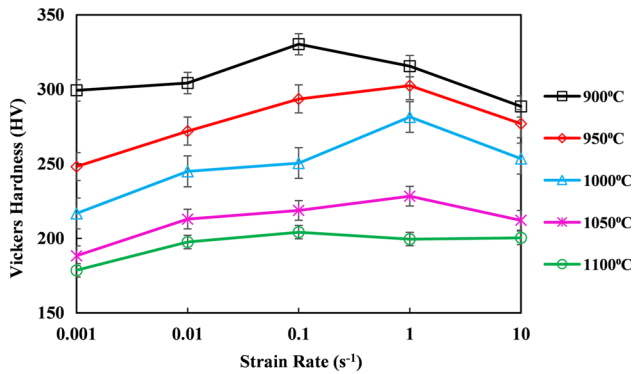

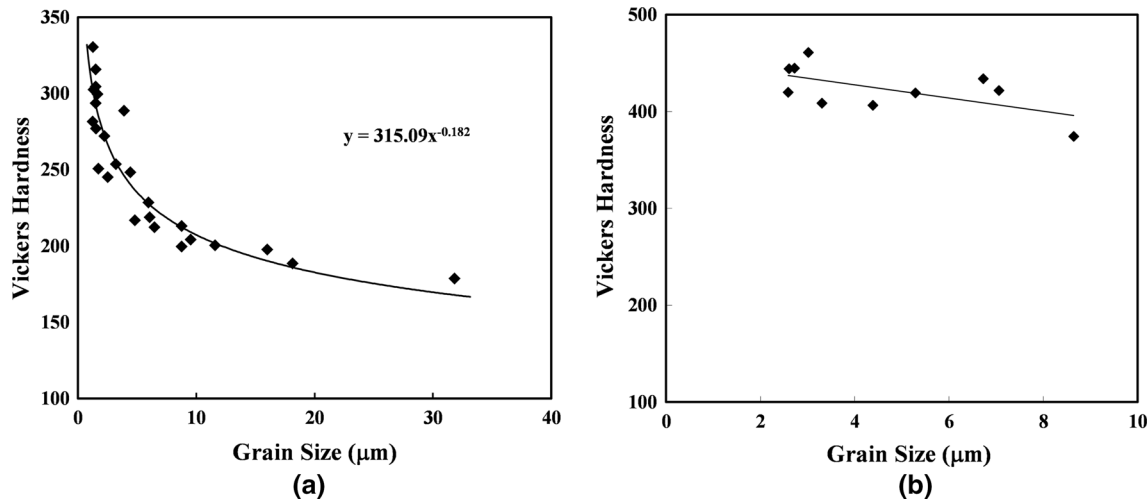Fig. 11—Microhardness variations for deformed specimens.

Fig. 12—Microhardness variation with grain size for (*a*) deformed specimens, (*b*) deformed and aged specimens.
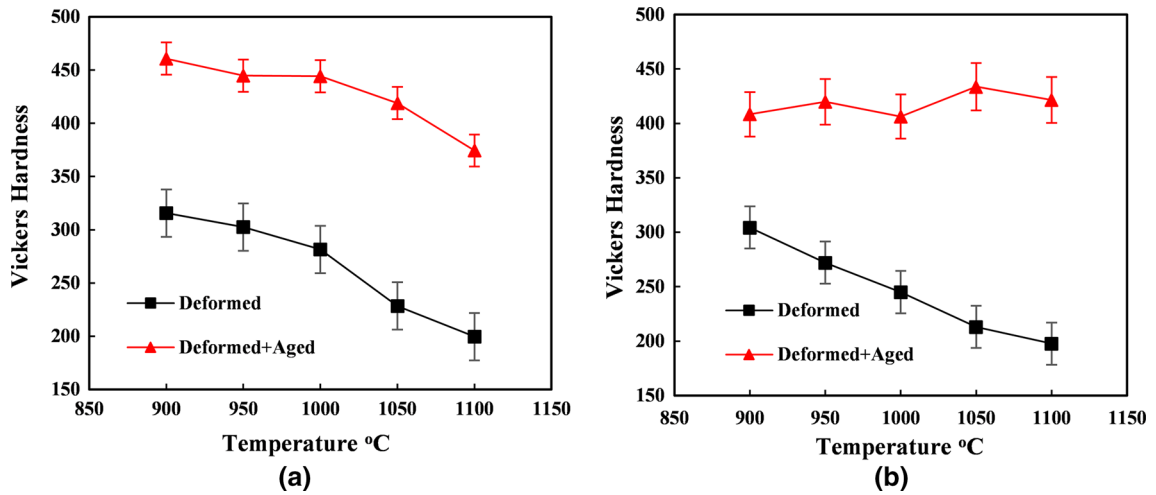
Fig. 13—Variation of Vickers microhardness with the temperature at strain rate (*a*) 0.01 s^{-1}, (*b*) 1 s^{-1}.

microstructural features clearly depict the processing history of the specimen. Deformation at the strain rate of 0.1 s^{-1} results in severe accumulation of lattice defects in the material. The accumulation of dislocations due to deformation is distinctly evident in the microstructure. The energy stored due to accumulation of defects drives the recovery and the recrystallization process during annealing.[46,54] In this case the specimen was subjected to deformation at 1050 °C, which promotes the recovery and recrystallization process dynamically. The formation of sub-grain boundaries indicated by arrows (Figure 14(a)) suggests the occurrence of recovery during deformation at high temperature. Regions with completely dynamically recrystallized grains were also evidenced in this specimen. The presence of dynamically recrystallized grains has been marked in the microstructure. The development of faceted grain and triple junctions can be clearly seen in Figures 14(c) and (d), which demonstrate the extent of DRX that occurred during deformation at 1050 °C.[60]

TEM analysis of the deformed and aged specimen is shown in Figure 15. Aging at 750 °C for 8 hour results in precipitation. Figure 15(a) shows the triple junction of three dynamically recrystallized grains with precipitates. The lenticular precipitates reported as γ'' having DO22—ordered structure were observed to be dominant in the microstructure.[61] The pair of bright-field and dark-field images of the lenticular precipitates have been shown in Figures 15(b) and (c). To establish the orientation relationship between ordered precipitates and the disordered matrix, the precipitates were observed in different zone axis. Figure 15(d) shows the precipitate observed in [110] zone and its corresponding diffraction and its schematic are provided in Figures 15(e) and (f), respectively. The intense reflections are from the matrix and the faint super lattice reflections are corresponding to the precipitate. The schematic of the SADP shows the orientation relationship between the matrix and the precipitate. The observation of precipitate in [111] zone and the diffraction and schematic of SADP is shown in Figures 15(g)

through (i). The analysis of the diffraction pattern reveals the orientation relationship between precipitate and matrix as $(001)\gamma''//\{001\}_{\text{matrix}}$ and $[100]\gamma''//\langle001\rangle_{\text{matrix}}$.

From the TEM micrographs, it is clear that due to deformation the specimen undergoes DRV and recrystallization which decreases the misorientation of the deformed specimen significantly (Figure 8(a)). Deformed and aged condition shows γ'' precipitates that increase the in-grain misorientation due to lattice distortion.[62,63] These precipitates also increase the hardness significantly (Figure 13). The increase in hardness for the deformed specimen is due to grain size only, whereas hardness of the aged specimen was dictated by the precipitates. This is the reason that there is no correlation between the grain size and hardness for the deformed + aged specimens.

The lowest temperature selected for the thermomechanical processing was 900 °C. The TTT diagram suggests that heat treatment at 900 °C induces precipitates in the Inconel alloy. However, the duration required to initiate the precipitates is about 20 minutes. In the present work, the total duration including heating (3 minutes, at the rate of 5 °C s^{-1}), annealing (5 minute) and deformation (12 minutes) were calculated to be maximum (20 minutes) for the lowest strain rate (0.001 s^{-1}) deformation and minimum (8 min) for the highest strain rate (10 s^{-1}) deformation. The duration required for complete deformation reduces with increasing strain rate. To confirm whether the deformation process induces precipitation, TEM analysis was carried out on the low-temperature (900 °C)-deformed specimens. Two specimens deformed at 0.001 s^{-1} for (i) 50 pct deformation and (ii) 60 pct deformation were subjected to TEM analysis and the results are provided in Figure 16. The microstructure of the 50 pct deformed specimen in Figures 16(a) and (b) illustrating the dynamically recrystallized grains and its SADP corresponding to Figure 16(b) is shown in Figure 16(c). The rearrangement of dislocations leading to the formation of low angle grain boundaries are distinctly evident in
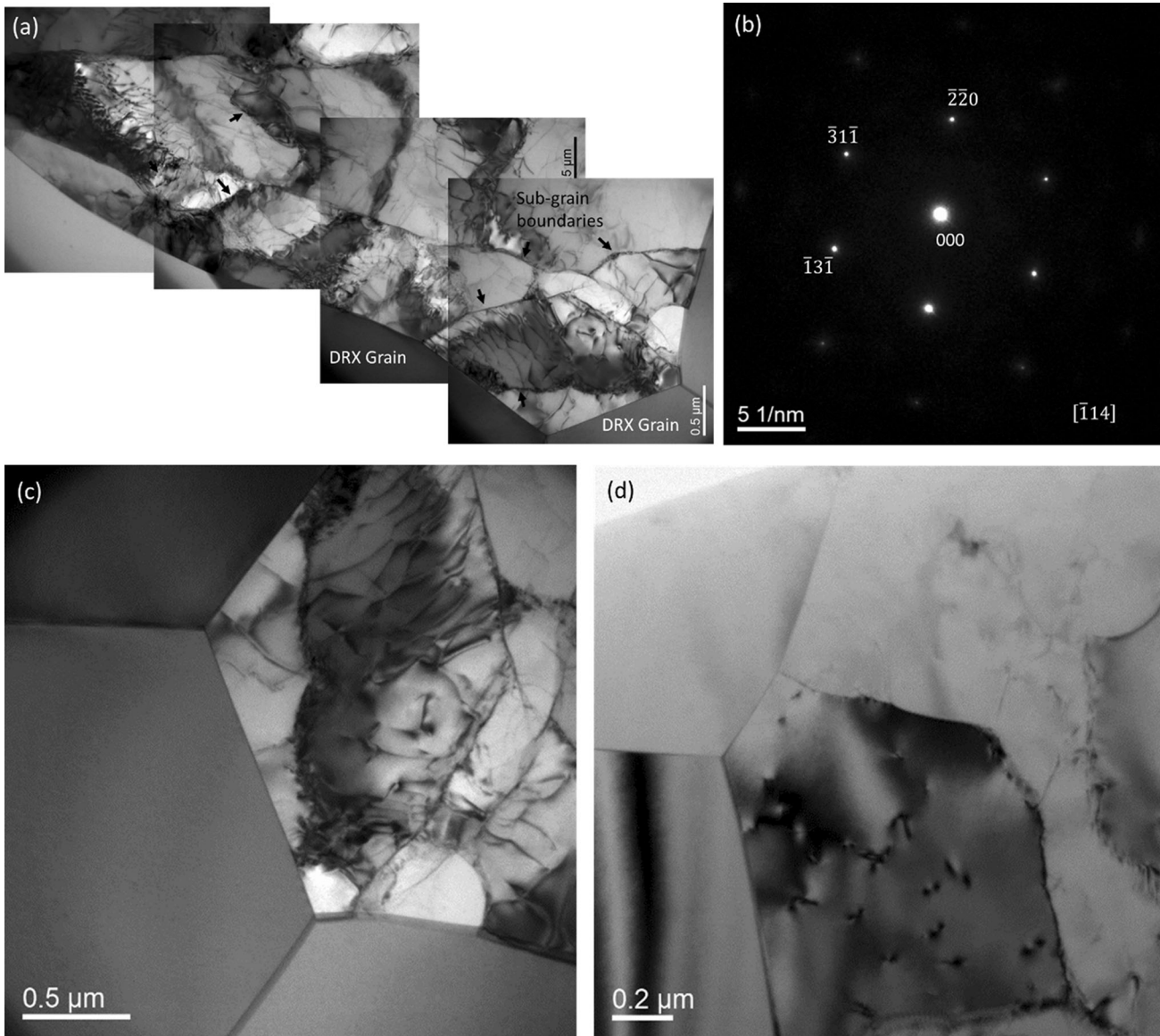
Fig. 14—TEM micrograph of the deformed specimen at 1050 °C and 0.1 s⁻¹. (*a*) DRX grain adjacent to highly deformed grain and its corresponding SADP (*b*), (*c*, *d*) faceted grains and triple junctions.

the microstructure. The microstructure specimen deformed to 60 pct (Figures 16(d) and (e)) also shows the dynamically recrystallized grains and dislocation structure. The diffraction pattern obtained from the region shown in Figure 16(e) is provided in Figure 15(f). As compared to the 50 pct deformation, the higher deformation (60 pct) microstructure showed a relatively higher fraction of dislocations. The microstructural analysis did not provide any evidence of precipitates in the microstructure. From the analysis, it is evident that low-temperature deformation does not favor any precipitation even at a lower strain rate. This is also confirmed through the microhardness analysis as the

values are nearly the same while varying the strain rate from 0.001 to 10 s⁻¹. Moreover, the hardness value corresponding to 0.001 s⁻¹ strain rate is marginally lower than the hardness value of 0.1 s⁻¹ strain rate. On the other hand, the hardness value of the deformed + aged specimen is significantly higher than that of the deformed specimen. These observations suggest that the deformation at the lowest strain rate at the lowest temperature is possibly devoid of precipitates, though it is close to the γ + Ni_3Nb curve in TTT diagram.

Thus, the thermomechanical processing parameters were designed initially to avoid precipitate development during hot deformation. The processing window for a
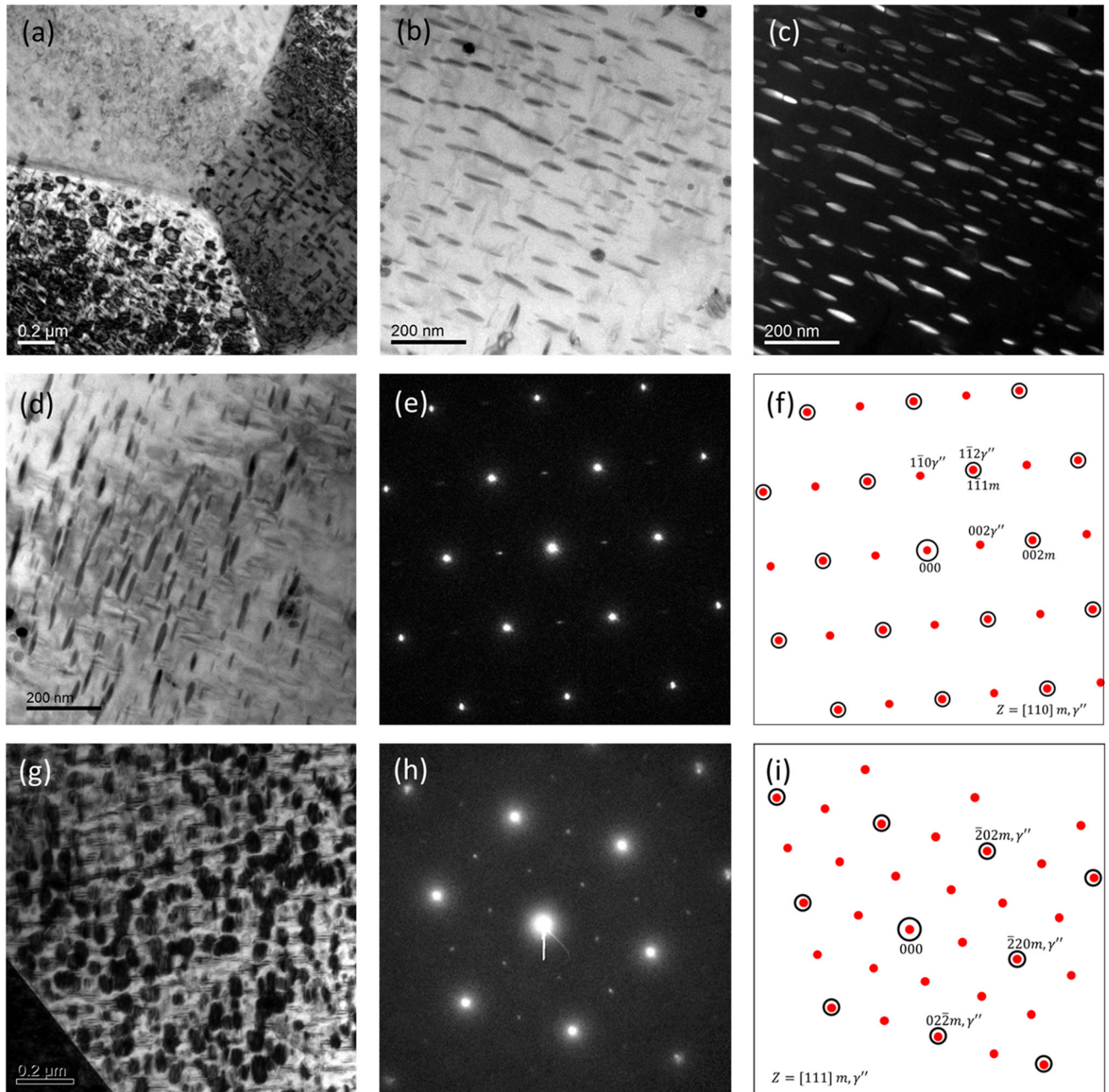
Fig. 15—TEM micrograph of deformed (1050 °C and 0.1 s^{-1}) and aged specimen. (*a*) BF image of γ'' precipitate, pair of (*b*) bright-field and (*c*) dark-field images of the lenticular precipitates. (*d* through *f*) The lenticular precipitate observed in [110] zone and its corresponding diffraction and schematic illustration. (*g* through *i*) The precipitate in [111] zone and its diffraction and schematic of SADP.

wide range of $\dot{\varepsilon}$, T, evidences a variety of microstructures such as DRX, deformed grains. The stable region of the processing map shows a higher efficiency for the DRX grain whereas the unstable region mostly shows highly deformed grains. Based on the stable and unstable domain of the processing map aging treatment were carried out on selected specimens. Interestingly, though aging does not have any significant effect on the microstructure morphology, higher hardness in the aged specimen highlights the development of precipitates. These precipitates influence the microstructural parameters such as local misorientation development and twin

fraction. Therefore, the overall objective of the manuscript was to link the microstructural features with processing conditions and precipitation behavior for different deformed microstructure, which is hitherto missing in the scientific literature.

IV. CONCLUSIONS

The processing map for high deformation of Inconel 718 was developed over the temperature range of 900 °C to 1100 °C and strain rate range of 0.001 to 10 s^{-1}.
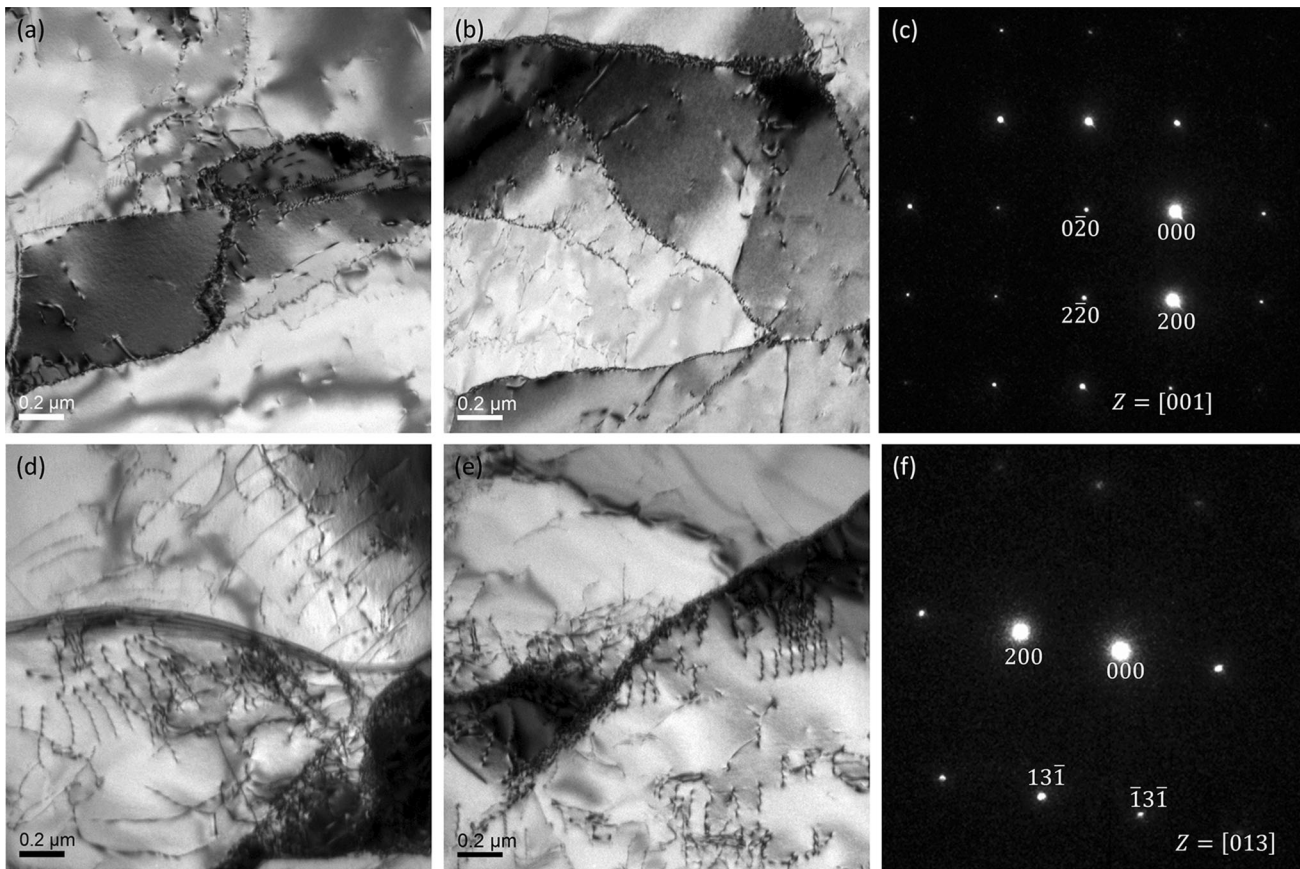
Fig. 16—Bright-field TEM micrograph of the deformed specimen at 900 °C and 0.001 s^{-1}. (*a* through *c*) after 50 pct deformation, and (*d* through *f*) after 60 pct deformation.

Further, aging treatment of these deformed specimens was performed at 750 °C for 8 hours. The following conclusions can be drawn from the present study:

1. Microstructure analysis of the wide $\dot{\varepsilon}, T$ suggests that, DRX is the major flow-softening mechanism at elevated temperatures (> 1000 °C) and favored by the slow strain rate deformation, whereas in the case of lower temperature deformation (950 °C to 1000 °C) a high GAM with partial DRX/DRV are the main flow-softening mechanism.

2. The maximum processing efficiency for Inconel 718 used in this study is found to be 0.4, that corresponds to the region of low strain rate, where considerable microstructural changes are observed in terms of DRX and grain growth.

3. The unstable zone as predicted by the dynamic material model lies in the low-temperature regime (900 °C to 1000 °C) and intermediate values of strain rate (1 s^{-1}). In this regime, highly deformed grains and partially recrystallized grains at grain boundaries were obtained.

4. Twin formation is significant at an elevated temperature. The maximum volume fraction of $\sum 3$ ($\langle 111 \rangle$, 60 deg) twin boundaries were observed at 1050 °C and strain rate of 0.1 to 1 s^{-1}. As the misorientation increases, twin fraction decreases

and the relation between them was found to be a power law.

5. Hardness and grain size results obtained after deformation are complementary to each other. Hardness increases with decreasing grain size. However, after aging treatment hardness increases and particularly for specimens deformed at 1 s^{-1}, it was found to be independent of grain size.

6. The increase in hardness is solely attributed to the grain size as no precipitates are observed in for two deformation temperatures 900 °C and 1050 °C. However, the higher hardness after aging at 750 °C for 8 hours, is due to the γ'' precipitates that are formed.

REFERENCES

1. E.A. Loria: *JOM*, 1992, vol. 44, pp. 33–36.
2. T.M. Pollock and S. Tin: *J. Propuls. Power*, 2006, vol. 22, pp. 361–74.
3. R.C. Reed: *The Superalloys Fundamentals and Applications*, 1st ed., Cambridge University Press, New York, 2006.
4. M.C. Chaturvedi and Y. Han: *Met. Sci.*, 1983, vol. 17, pp. 145–49.
5. R. Cozar and A. Pineau: *Metall. Trans.*, 1973, vol. 4, pp. 47–59.
6. S. Azadian, L.-Y. Wei, and R. Warren: *Mater. Charact.*, 2004, vol. 53, pp. 7–16.
7. H. Yuan and W.C. Liu: *Mater. Sci. Eng. A*, 2005, vol. 408, pp. 281–89.

8. A. Agnoli, M. Bernacki, R. Logé, J.-M. Franchet, J. Laigo, and N. Bozzolo: *Metall. Mater. Trans. A*, 2015, vol. 46A, pp. 4405–21.
9. M. Azarbarmas, M. Aghaie-Khafri, J.M. Cabrera, and J. Calvo: *Mater. Sci. Eng. A*, 2016, vol. 678, pp. 137–52.
10. M. Sundararaman, P. Mukhopadhyay, and S. Banerjee: *Acta Metall.*, 1988, vol. 36, pp. 847–64.
11. Y.V.R.K. Prasad and N. Ravichandran: *Bull. Mater. Sci.*, 1991, vol. 14, pp. 1241–48.
12. S. Guo, D. Li, H. Pen, Q. Guo, and J. Hu: *J. Nucl. Mater.*, 2011, vol. 410, pp. 52–58.
13. X.M. Chen, Y.C. Lin, D.X. Wen, J.L. Zhang, and M. He: *Mater. Des.*, 2014, vol. 57, pp. 568–77.
14. Q.M. Guo, D.F. Li, and S.L. Guo: *Mater. Manuf. Process.*, 2012, vol. 27, pp. 990–95.
15. A. Nowotnik: Superalloys 2008 (Eleventh International Symposium)*TMS*, 2008, vol. 2008, pp. 709–17.
16. M.C. Somani, K. Muraleedharan, N.C. Birla, V. Singh, and Y.V.R.K. Prasad: *Metall. Mater. Trans. A*, 1994, vol. 25A, pp. 1693–1702.
17. P.J. Wray: *J. Appl. Phys.*, 1969, vol. 40, pp. 4018–29.
18. R. Raj: *Metall. Mater. Trans. A*, 1981, vol. 12A, pp. 1089–97.
19. Y.V.R.K. Prasad, H.L. Gegel, S.M. Doraivelu, J.C. Malas, J.T. Morgan, K.A. Lark, and D.R. Barker: *Metall. Mater. Trans. A*, 1984, vol. 15A, pp. 1883–92.
20. S.V.S. Narayana Murty, M.S. Sarma, and B.N. Rao: *Metall. Mater. Trans. A*, 1997, vol. 28A, pp. 1581–82.
21. J.C. Malas and V. Seetharaman: *JOM*, 1992, vol. 44, pp. 48–13.
22. S.L. Semiatin and G.D. Lahoti: *Metall. Mater. Trans. A*, 1981, vol. 12A, pp. 1705–17.
23. F. Montheillet, J.J. Jonas, and K.W. Neale: *Metall. Mater. Trans. A*, 1996, vol. 27A, pp. 232–35.
24. X. Ma, W. Zeng, K. Wang, Y. Lai, and Y. Zhou: *Mater. Sci. Eng. A*, 2012, vol. 550, pp. 131–37.
25. Y.V.R.K. Prasad, K. P. Rao, and S.Sasidhar: *Hot Working Guide: A Compendium of Processing Maps*, 2nd ed., ASM International, 2015.
26. F. Sui, L. Xu, L. Chen, and X. Liu: *J. Mater. Process. Technol.*, 2011, vol. 211, pp. 433–40.
27. S. Medeiros, Y.V.R. Prasad, W. Frazier, and R. Srinivasan: *Mater. Sci. Eng. A*, 2000, vol. 293, pp. 198–207.
28. N. Srinivasan and Y.V.R.K. Prasad: *Metall. Mater. Trans. A*, 1994, vol. 25A, pp. 2275–84.
29. D. Wen, Y.C. Lin, H.-B. Li, X. Chen, J. Deng, and L. Li: *Mater. Sci. Eng. A*, 2014, vol. 591, pp. 183–92.
30. H. Zhang, K. Zhang, Z. Lu, C. Zhao, and X. Yang: *Mater. Sci. Eng. A*, 2014, vol. 604, pp. 1–8.
31. Y.C. Lin, X.-M. Chen, D. Wen, and M. Chen: *Comput. Mater. Sci.*, 2014, vol. 83, pp. 282–89.
32. X.-M. Chen, Y.C. Lin, M. Chen, H. Li, D. Wen, J. Zhang, and M. He: *Mater. Des.*, 2015, vol. 77, pp. 41–49.
33. H.Y. Zhang, S.H. Zhang, M. Cheng, and Z.X. Li: *Mater. Charact.*, 2010, vol. 61, pp. 49–53.
34. A. Thomas, M. El-Wahabi, J.M. Cabrera, and J.M. Prado: *J. Mater. Process. Technol.*, 2006, vol. 177, pp. 469–72.
35. G.A. Rao, M. Kumar, M. Srinivas, and D.S. Sarma: *Mater. Sci. Eng. A*, 2003, vol. 355, pp. 114–25.
36. A. Chamanfar, L. Sarrat, M. Jahazi, M. Asadi, A. Weck, and A.K. Koul: *Mater. Des.*, 2013, vol. 52, pp. 791–800.
37. F. Theska, A. Stanojevic, B. Oberwinkler, S.P. Ringer, and S. Primig: *Acta Mater.*, 2018, vol. 156, pp. 116–24.
38. N. Bozzolo, N. Souaï, and R.E. Logé: *Acta Mater.*, 2012, vol. 60, pp. 5056–66.
39. T. Al-Samman and G. Gottstein: *Mater. Sci. Eng. A*, 2008, vol. 490, pp. 411–20.
40. Y. Wang, W.Z. Shao, L. Zhen, and B.Y. Zhang: *Mater. Sci. Eng. A*, 2011, vol. 528, pp. 3218–27.
41. H. Jiang, J. Dong, M. Zhang, L. Zheng, and Z. Yao: *J. Alloys Compd.*, 2015, vol. 647, pp. 338–50.
42. C.A. Dandre, S.M. Roberts, R.W. Evans, and R.C. Reed: *Mater. Sci. Technol.*, 2000, vol. 16, pp. 14–25.
43. S.I. Wright, M.M. Nowell, S.P. Lindeman, P.P. Camus, M. De Graef, and M.A. Jackson: *Ultramicroscopy*, 2015, vol. 159, pp. 81–94.
44. M. Zouari, N. Bozzolo, and R.E. Loge: *Mater. Sci. Eng. A*, 2016, vol. 655, pp. 408–24.
45. R. Gujrati, C. Gupta, J.S. Jha, S. Mishra, and A. Alankar: *Mater. Sci. Eng. A*, 2019, vol. 744, pp. 638–51.
46. T. Sakai, A. Belyakov, R. Kaibyshev, H. Miura, and J.J. Jonas: *Prog. Mater. Sci.*, 2014, vol. 60, pp. 130–207.
47. G. He, F. Liu, L. Huang, Z. Huang, and L. Jiang: *J. Alloys Compd.*, 2017, vol. 701, pp. 909–19.
48. J.J. Jonas, C.M. Sellars, and W.J.M. Tegart: *Metall. Rev.*, 1969, vol. 14, pp. 1–24.
49. S. Mishra, K. Narasimhan, and I. Samajdar: *Mater. Sci. Technol.*, 2007, vol. 23, pp. 1118–26.
50. S. Mandal, S.K. Mishra, A. Kumar, I. Samajdar, P.V. Sivaprasad, T. Jayakumar, and B. Raj: *Philos. Mag.*, 2008, vol. 88, pp. 883–97.
51. H. Ziegler: vol. 4, Wiley, New York, 1963, pp. 93–113.
52. Y.V.R.K. Prasad and T. Seshacharyulu: *Mater. Sci. Eng. A*, 1998, vol. 243, pp. 82–88.
53. M. Calcagnotto, D. Ponge, E. Demir, and D. Raabe: *Mater. Sci. Eng. A*, 2010, vol. 527, pp. 2738–46.
54. J. Humphreys and G.S. Rohrer: *Recrystallization and Related Annealing Phenomena*, 3rd ed., Elsevier, Amsterdam, 2017.
55. Y.C. Lin, M. Chen, and J. Zhong: *Mech. Res. Commun.*, 2008, vol. 35, pp. 142–50.
56. E.I. Poliak and J.J. Jonas: *ISIJ Int.*, 2003, vol. 43, pp. 684–91.
57. S. Mandal, A.K. Bhaduri, and V. Subramanya Sarma: *Metall. Mater. Trans. A*, 2011, vol. 42A, pp. 1062–72.
58. F. Chen, J. Liu, H. Ou, B. Lu, Z. Cui, and H. Long: *Mater. Sci. Eng. A*, 2015, vol. 642, pp. 279–87.
59. D.J. Abson and J.J. Jonas: *Met. Sci. J.*, 1970, vol. 4, pp. 24–28.
60. D. Wen, Y.C. Lin, J. Chen, X. Chen, J. Zhang, Y. Liang, and L. Li: *J. Alloys Compd.*, 2015, vol. 618, pp. 372–79.
61. M. Miller: *Micron*, 2001, vol. 32, pp. 757–64.
62. J. Oblak, D. Duvall, and D. Paulonis: *Mater. Sci. Eng.*, 1974, vol. 13, pp. 51–56.
63. I.J. Moore, M.G. Burke, N.T. Nuhfer, and E.J. Palmiere: *J. Mater. Sci.*, 2017, vol. 52, pp. 8665–80.